

High-rate decoupled water electrolysis system integrated with α -MoO₃ as a redox mediator with fast anhydrous proton kinetics

Zihan Ma

The University of Tokyo <https://orcid.org/0000-0002-4169-0605>

Xiaofei Lu

The University of Tokyo

Sunghyun Park

The University of Tokyo

Tatsuya Shinagawa

The University of Tokyo <https://orcid.org/0000-0002-5240-7342>

Masashi Okubo

Waseda University

Kazuhiro Takanabe

The University of Tokyo

Atsuo Yamada (✉ yamada@chemsys.t.u-tokyo.ac.jp)

The University of Tokyo <https://orcid.org/0000-0002-7880-5701>

Article

Keywords:

Posted Date: May 25th, 2022

DOI: <https://doi.org/10.21203/rs.3.rs-1655734/v1>

License:  This work is licensed under a Creative Commons Attribution 4.0 International License.

[Read Full License](#)

Abstract

Hydrogen is a promising alternative to fossil fuels that can reduce greenhouse gas emissions. Decoupled water electrolysis system using a reversible proton storage redox mediator, where the oxygen evolution reaction and hydrogen evolution reaction are separated in time and space, is an effective approach to produce hydrogen gas with high purity, high flexibility, and low cost. To realize a fast hydrogen production in such a system, a redox mediator capable of releasing proton rapidly is required. Herein, α - MoO_3 , with an ultrafast proton transfer property that can be explained by a dense hydrogen bond network in the lattice oxygen arrays of H_xMoO_3 , was examined in this work as a high-rate redox mediator for fast hydrogen production in acidic electrolytes. The α - MoO_3 redox mediator shows both a large capacity of 204 mAh g^{-1} and fast hydrogen production at a current rate of 1 A cm^{-2} (100 A g^{-1}), outperforming most of the previously reported solid-state redox mediators.

Introduction

Hydrogen, a clean energy carrier, plays a significant role in achieving a sustainable society, which could effectively store intermittent energy generated by renewable energy sources (e.g., wind and solar) and decrease CO_2 emission as an important chemical feedstock for various industrial processes (e.g., NH_3 and steel)¹. Among all hydrogen production approaches, water electrolysis with only one byproduct, O_2 , is considered the most versatile way.² In conventional water electrolysis systems, hydrogen evolution reaction (HER) is coupled with oxygen evolution reaction (OER) that are separated by an ion-exchange membrane. At steady state, the rates of these two reactions must be identical. There are some issues to be resolved, such as (1) the overall performance is pinned by the sluggish kinetics of the OER, (2) the high capital cost for polymer electrolyte water electrolyzers, (3) potential product gas crossover that causes low H_2 purity.³ Therefore, decoupled water splitting systems have been designed to enable more flexible and more efficient hydrogen production in various pH conditions.⁴⁻⁶ In a decoupled water splitting system, a redox mediator plays the key role to store protons during OER and release the protons during HER, meanwhile, the valence state of a redox center (usually transition metals) changes reversibly to balance the charge transfer.

In 2013, water-soluble polyoxometalate $\text{H}_3\text{PMo}_{12}\text{O}_{40}$ was firstly reported as a homogeneous redox mediator, where it reversibly turns to $\text{H}_5\text{PMo}_{12}\text{O}_4$ upon proton storage during the OER process, accompanied by the partial reduction of Mo(VI) to Mo(V), and is re-oxidized to $\text{H}_3\text{PMo}_{12}\text{O}_{40}$ during HER process⁷. However, a proton exchange membrane is still required in the system to separate the redox mediator solution from the electrolyte. Later, many insoluble solid-state redox mediators were reported⁸⁻¹¹. They play the roles of both a reversible proton host and a separator. Up to now, the most studied solid-state redox mediator is nickel hydroxide $\text{Ni}(\text{OH})_2$, whose working principle is the same as that in a positive electrode for commercial Ni-metal hydride (MH) or Ni-Cd batteries.¹² In a typical electrolyte of an aqueous alkaline solution (e.g. 1 M KOH), upon proton extraction accompanied with HER ($4\text{H}_2\text{O} + 4\text{e}^- \rightarrow 2\text{H}_2 +$

4OH^-), $\text{Ni}(\text{OH})_2$ turns to NiOOH and reversibly turns back to $\text{Ni}(\text{OH})_2$ after re-insertion of protons during OER process ($4\text{OH}^- \rightarrow \text{O}_2 + 2\text{H}_2\text{O} + 4\text{e}^-$). However, the redox potential of $\text{Ni}^{3+}/\text{Ni}^{2+}$ (1.36 V vs. reversible hydrogen electrode (RHE), $\text{pH} = 14$) in $\text{Ni}(\text{OH})_2$ is outside the water redox potential window (OER at 1.23 V vs. RHE)^{11,13}. Although the much larger kinetic overpotential of OER over $\text{Ni}(\text{OH})_2$ enables the sole oxidation of $\text{Ni}(\text{OH})_2$ at low rates, simultaneous oxygen evolution would occur at higher rates as the overpotential of $\text{Ni}^{3+}/\text{Ni}^{2+}$ redox increases¹⁴, leading to poor gas purity of the hydrogen product. To achieve a high-rate hydrogen generation, a Prussian (Turnbull's) blue analog (TBA), $\text{Cu}[\text{Fe}(\text{CN})_6]_{2/3} \cdot 3.4\text{H}_2\text{O}$ (CuFe-TBA) based on $\text{Cu}^{2+}/\text{Cu}^+$ and $\text{Fe}^{3+}/\text{Fe}^{2+}$ redox couples was proposed as a high-rate redox mediator due to its fast proton transfer property.¹⁵ The fast proton kinetics can be explained by a Grotthuss topochemistry in the hydrogen-bond network formed by structural water^{16,17}. The capacity of CuFe-TBA is however intrinsically small (81 mAh g^{-1} at 0.5 A g^{-1}) due to the carriage of much extra weight so that large amounts of redox mediator would be required in practical applications, which would inflate both cost and inefficiency.

$\alpha\text{-MoO}_3$, with a unique bilayered structure and multivalent redox center Mo (VI, V, IV, III) (**Figure 1**), has been studied as a proton host material with fast kinetics and large capacities for battery applications.^{18–20} Recently, the science behind the fast proton transfer properties of $\alpha\text{-MoO}_3$ was unveiled by Yamada group²¹. Due to the dense oxide-ion arrays of MoO_3 (O-O distance $< 3 \text{ \AA}$), inserted proton can chemically bond with one lattice oxygen and form one or more hydrogen bonds with other lattice oxygens, building a dense hydrogen bond network. This environment highly resembles that in water (average O-O distance: 3.1 \AA) where protons can be transported with Grotthuss mechanism. Therefore, even without structural water, protons can be transferred with an ultralow energy barrier of $\sim 0.13 \text{ eV}$ in dense oxide-ion arrays of $\alpha\text{-MoO}_3$, making it a promising candidate as a redox mediator with comparable rate capability with TBAs (diffusion barrier $\sim 0.15 \text{ eV}$)¹⁷ and a much larger capacity (theoretically >3 times). In this work, utilizing model electrodes of IrO_x and Pt as an anode and a cathode, respectively, we investigated the $\alpha\text{-MoO}_3$ as a high-rate, large-capacity redox mediator for decoupled water electrolysis to produce pure hydrogen in a membrane-free system. Our electrochemical tests revealed that $\alpha\text{-MoO}_3$ could realize a fast hydrogen production of up to ca. $4 \text{ mmol H}_2/\text{g}(\text{MoO}_3)$ within 8 seconds.

Results And Discussion

Fast deprotonation of MoO_3 enabled by facile anhydrous proton transfer

A prototype of the decoupled water electrolysis is illustrated in **Figure 1**, involving the OER over IrO_x and H^+ intercalation in $\alpha\text{-MoO}_3$ (step 1), as well as the subsequent hydrogen production on Pt conjugated with the deprotonation of $\text{H}_{2.5}\text{MoO}_3$ (step 2). These two processes are carried out alternately to produce pure hydrogen without separation in a membrane-free system.

α -MoO₃ was synthesized by a hydrothermal method (See Methods). The high purity and crystallinity of as-prepared product was confirmed with the powder diffraction pattern, and the morphology was confirmed by scanning electron microscope (SEM) to be micron-sized rods (**Figure S1**). The MoO₃ electrode was prepared by casting a slurry consisting of α -MoO₃, conductive carbon, and binder on a carbon cloth. Before testing the gas production properties, we first explored the suitable identity and concentration of electrolyte to suppress the dissolution of α -MoO₃ by limiting the free water amount¹⁸. As a result, phosphoric acid was chosen since it is a relatively weak acid so that the corrosion of cell parts is alleviated even at the high concentration of 10 M (pH 0.2~0.5)²². Although α -MoO₃ was reported to be capable of delivering both large capacities and high rates even with a loading level of > 90 mg cm⁻²,²³ the loading level was controlled to ~10 mg cm⁻² in our experiments to enable the lab-scale measurements to demonstrate high current up to 100 A g⁻¹ (**Figure S2**). An IrO_x coated Ti felt²⁴ and a platinized platinum (Pt/Pt mesh)²⁵ were fabricated as the OER and HER electrodes, respectively, prepared by the reported electrochemical deposition protocols.²⁶ The system is also feasible in H₂SO₄-based electrolyte (**Figure S3**); however, long-term cycling in low concentration electrolytes requires further optimizations to suppress the dissolution of α -MoO₃. Optimization approaches include increasing the electrolyte concentration, introducing electrolyte additives^{27,28} and coating electrode surface with protecting layers^{29,30}.

The redox properties of the mediator α -MoO₃ were investigated by electrochemical characterization of the as-prepared electrodes. **Figure 2a** shows the cyclic voltammetry (CV) curves measured for α -MoO₃ at a scan rate of 1 mV s⁻¹ in an aqueous solution of 10 mol L⁻¹ (M) H₃PO₄. To suppress the parasitic OER or HER on the α -MoO₃ electrode, the cutoff potentials were set at -0.30 V and 0.45 V versus Ag/AgCl, so that the water electrolysis reactions on α -MoO₃ electrode are suppressed kinetically. The CV curves of the α -MoO₃ electrode show four cathodic and two anodic peaks in the first cycle (pale blue line in **Figure 2a**); however, it become symmetric in the subsequent cycles, showing two pairs of redox peaks at around -0.3 and 0.2 V versus Ag/AgCl. The difference between the CV curves in the first cycle and the subsequent cycles is because that part of the intercalated protons (~1 H⁺ per MoO₃) in the first protonation process were trapped in α -MoO₃ structure due to the lack of fast diffusion channels so that only ~1.5 proton per α -MoO₃ is reversible in the subsequent cycles with fast rate (H₁MoO₃ \rightleftharpoons H_{2.5}MoO₃). The remaining 1.0 H⁺ can be extracted when applying a constant voltage at the end of deprotonation for 3 h (**Figure S4**). The CV curves share large resemblances with that in a 32 mol kg⁻¹ (m) ZnCl₂ + 1 m P₂O₅ electrolyte in our previous study²¹, indicating the same H⁺ intercalation mechanism in α -MoO₃. Additionally, the CV data of HER (red line) and OER (black line) using model Pt/Pt mesh and IrO_x/Ti felt electrodes were also measured in the same electrolyte and appended in **Figure 2a** for comparison.

The kinetics of proton transfer in α -MoO₃ could significantly affect the performance of decoupled water electrolysis. The fast deprotonation properties (coupled with HER) of the α -MoO₃ electrode (0.4 cm², 4

mg MoO₃) were tested with different current densities from 4 A g⁻¹ to 100 A g⁻¹. The results are shown in **Figure 2b**. The cut-off potentials at different current densities were adjusted to allow sufficient deprotonations (**Figure 2b inset**). About 77% of the specific capacity at 4 A g⁻¹ is available at the fast deprotonation rate of 100 A g⁻¹. About 90% of the initial capacity is retained after cycling at each rate. The α-MoO₃ lattice response to galvanostatic proton intercalation was monitored with *in situ* X-ray diffraction (XRD) method (MoO₃→H_{2.5}MoO₃→HMoO₃, **Figure 2c**). The structure evolution is asymmetric but reversible, consistent with the case in a 32 m ZnCl₂ + 1 m P₂O₅ electrolyte²¹. Note that the interlayer distance (corresponding 020 peak) exhibits neglectable changes upon protonation, indicating barely any water co-insertion happens. These performance results indicate the stability of the α-MoO₃ framework against repeated proton insertion and extraction as well as the fast proton diffusion therein H_xMoO₃ (1.0 ≤ x ≤ 2.5). Overall, these findings demonstrate the fast proton transfer in α-MoO₃, which will be utilized as a redox mediator to decouple the acid water electrolysis in the following sections.

Efficiency and purity of gas production

Knowing the electrochemical behavior of α-MoO₃ in 10 M H₃PO₄, the chronopotentiometry (CP, potential vs. time) technique was utilized to examine the performance of decoupled water electrolysis in a membrane-free one-chamber cell containing 30 mL electrolyte. To evaluate the gas production efficiency and gas purity, in-line mass spectra (MS) was adopted to analyze the effluent gas products with Ar carrier gas (50 mL min⁻¹). To check the validity of this system, a current of 20 mA was applied on the working electrode (OER/HER electrode, 1 cm²), where the MoO₃ redox mediator electrode (10 mg MoO₃ on a carbon cloth of 1 cm²) works as a counter electrode and Ag/AgCl (in a saturated KCl aqueous solution) was employed as a reference electrode (ca. -0.16 V vs. SHE in 10 M H₃PO₄), respectively.

The chronopotentiometry results of electrodes in conjunction with the in-line monitoring of generated products was recorded to validate our hypothesis for the decoupled water electrocatalysis. As demonstrated in **Figure 3a**, in OER mode (step 1) (step time: 400 s, corresponding to 2.22 mAh), the potential of OER catalyst electrode kept almost constant at ca. 1.57 V vs. Ag/AgCl while the potential of α-MoO₃ decreased from ca. 0.16 V to -0.28 V vs. Ag/AgCl upon proton insertion, showing two plateaus, consistent with the two redox peaks in the CV curves. The oxygen gas product was detected immediately after the current was applied, the oxygen concentration increased gradually as O₂ gas accumulated in the flowing system and reached the peak at the end of the OER step. The MS signal shows an unavoidable delay in time due to partial dissolving of gas product into electrolyte and the dead volume before reaching to the MS inlet. Accordingly, a rest time of ca. 400 s is necessary to collect all the gas product. The total gas production amount (ca. 19.7 μmol) was calculated by integrating the area of MS signal. The Faradaic efficiency (amount of gas detected/theoretical gas production based on charge transfer of 8 C, 20.7 μmol in this case) of oxygen evolution is approximately 95%. The origin of the loss in Faradaic efficiency could be attributed to incomplete gas collection originated from O₂ dissolution in the electrolyte

and redox events on the OER electrode. The occurrence of oxygen reduction reaction (ORR) on MoO₃ electrode can be ruled out because of the absence of cathodic currents in CV scans even under pure oxygen atmosphere (**Figure S5**). Note that the cut-off potential should be well-controlled since the overprotonation of MoO₃ would lead to parasitic HER (**Figure S6**).

Then the system was switched to HER mode. Similar to the OER step, the potential of HER catalyst electrode kept constant at ca. -0.21 V vs. Ag/AgCl while the potential of α -MoO₃ increased from ca. -0.18 V to 0.33 V vs. Ag/AgCl upon deprotonation. The total hydrogen gas production detected by MS was estimated to be 40.2 μ mol, about twice amount of oxygen produced in step 1, with a Faradaic efficiency of ca. 97%. Also, separate experiment confirmed that no hydrogen oxidation reaction (HOR) occurred on α -MoO₃ electrode even in a pure hydrogen atmosphere (**Figure S5**). The remained protons that were tracked in H_xMoO₃ structure kinetically can be released and produces ca. 50% additional hydrogen gas on HER electrode if a constant potential of 0.5 V vs. Ag/AgCl is applied to the α -MoO₃ electrode (**Figure S7**).

Overall, these results proved that the α -MoO₃ redox mediator works effectively and efficiently as a proton host, decoupling the OER and HER processes in two steps with average voltages of 1.58 V and 0.32 V, respectively, in contrast with 1.78 V in a coupled case. Incremental overpotential as low as ~0.12 V demonstrates the kinetically facile redox properties as well as low internal resistance of α -MoO₃ nature. As expected, no impurity gas other than Ar carrier gas was detected in both OER and HER steps, indicating a nearly 100% gas purity for both oxygen and hydrogen products.

High-rate hydrogen gas production with *α -MoO₃ redox mediator*

To reveal the operational stability of this decoupled water electrolysis system, the cycle performance at fixed HER rate were examined. Time-course changes of the potential of electrodes and corresponding hydrogen and oxygen productions in 20 consecutive OER and HER cycles are illustrated in **Figure 4a**. The current was increased to 80 mA to realize fast HER steps while it remained 40 mA for sluggish OER steps. In between each HER/OER step, a break of 500 s was introduced to distinguish the gas products. The potentials of OER and HER electrodes remain almost constant at ca. 1.6 V and -0.3 V vs. Ag/AgCl, respectively, in each cycle while the potential of α -MoO₃ swings in the range between -0.3 V and 0.4 V upon repeated (de)protonation. The concentration of H₂ increased sharply during the HER step and then decreased after the current becomes zero, with a Faradaic efficiency of 94%-99%. The signal of O₂ also increases during each OER step as expected.

To further illustrate the operational flexibility, the performance of the system was evaluated at various currents of 20, 40, 80, 160, 320, 640 and 1000 mA, respectively. The corresponding potential curves of α -MoO₃ and HER electrode are plotted in **Figure 4b**, and the responsive curves of generated hydrogen in MS as well as the calculated amount are shown in **Figure 4c**. Interestingly, large current rates up to 1 A was achieved with high Faradaic efficiency to H₂ of 96%. At all rates investigated in this study, the Faradaic

efficiencies exhibited > 95% (**Figure 4c inset**), indicating both high rate and efficient hydrogen production in the proposed prototype.

To compare the performance of α - MoO_3 as a solid-state redox mediator with benchmark materials, we tested the performances of $\text{Ni}(\text{OH})_2$ and CuFe-TBA using the same set-up. The battery grade $\text{Ni}(\text{OH})_2$ was purchased and the CuFe-TBA was prepared by a co-precipitation method. Both materials have high purity and crystallinity as evidenced by X-ray diffraction patterns (**Figure S8**). The SEM pictures in **Figure S1** and **S8** reveals that the morphology, especially particle size of pristine MoO_3 , $\text{Ni}(\text{OH})_2$ and CuFe-TBA powders varies largely, which might bring major differences in their electrochemical performances. Therefore, a 30-min ball-milling process was conducted to all three powders with carbon additives to decrease the particle size as well as increasing the electric conductivity before electrochemical characterizations. As shown in **Figure S9**, the primary particle size of $\text{Ni}(\text{OH})_2$ and CuFe-TBA were reduced to < 0.5 μm while the ball-milled MoO_3 particle is slightly larger. The XRD patterns of the ball-milled samples reveal that all three samples remained high crystallinity even after ball-milling. Thus, the ball-milled powders were used to prepare the electrodes and conduct electrochemical measurements. The CV curves of $\text{Ni}(\text{OH})_2$ electrode in an electrolyte of 1 M KOH at a scan rate of 1 mV s^{-1} can be found in **Figure S10a**, the $\text{Ni}^{3+}/\text{Ni}^{2+}$ oxidative peak is largely overlapped with OER in the first cycle and gradually becomes more pronounced after an activation process of 5 cycles, which is consistent with previous report.¹¹ Also, similar to previous studies^{31,32}, $\text{Ni}(\text{OH})_2$ delivered a large discharge capacity of 271 mAh g^{-1} at the current rate of 2 A g^{-1} (20 mA), reaching 92% of its theoretical capacity. However, the fast deprotonation properties of $\text{Ni}(\text{OH})_2$ as a redox mediator are barely tested before. When the scan rate increases, the overlap of oxidative peak becomes more severe (**Figure S10b**). Indeed, the MS detected evident parasitic oxygen evolution and Faradic efficiencies decreased remarkably in HER steps at current rates of > 160 mA, indicating the limited high-rate properties of $\text{Ni}(\text{OH})_2$ without special electrode configurations such as carbon nanotube additives (**Figure S11**). On the other hand, the CV curves of CuFe-TBA in 10 M H_3PO_4 electrolyte shows no evident overlap with HER/OER (**Figure S12a**). Consistent with the literatures^{15,17}, CuFe-TBA shows an outstanding deprotonation rate capability, however, the capacities are remarkably lower than that of α - MoO_3 , (74 mAh g^{-1} , in contrast with 260 mAh g^{-1} of MoO_3 at 4 A g^{-1}) (**Figure S12b**) with a hydrogen production amount of 10-14 μmol at rates from 20-640 mA (**Figure S13**). The quantitative estimation of generated H_2 over 10 mg of various mediators by MS was plotted as a function of the applied current density, shown in **Figure 5**. These results revealed that both benchmark materials produce less hydrogen at high current densities. More specifically, the MoO_3 and $\text{Ni}(\text{OH})_2$ could produce large amount of hydrogen at low current density (less than 4 A g^{-1}), delivering > 4 mmol H_2 per gram mediators. Then the two kinds of materials give different pictures with the increasing current density (> 4 A g^{-1}). The amount of generated hydrogen over α - MoO_3 slightly decreased, maintaining ca. 87% of the original amount even at 100 A g^{-1} . On the contrary, over $\text{Ni}(\text{OH})_2$, it decreased to ca.70% of the original one at just 16 A g^{-1} and further increase of current rates would lead to unacceptable hydrogen gas purity due to parasitic OER. Regarding the CuFe-TBA, it could preserve ca. 86% of the amount of

hydrogen production over the range of the investigated current density (4-64 A g⁻¹). Its total amount of hydrogen production is only one third of that over α -MoO₃.

The unique proton transfer based on hydrogen bond networks in solid structures for fast proton transport in α -MoO₃ and CuFe-TBA could rationalize the persisting hydrogen generation under high current densities. Indeed, the proton diffusion barriers in α -MoO₃ and CuFe-TBA are < 0.3 eV^{17,21}, resembling that in liquid water *via* the Grotthuss mechanism (< 0.4 eV), thanks to the dense oxide ion arrays (O-O distance < 3 Å) in α -MoO₃ and abundant structural water in CuFe-TBA that facilitate the proton hopping. In contrast, Ni(OH)₂, with O-O distance of ca. 3.18 Å, exhibit a much larger proton diffusion barrier of > 0.6 eV³³. The unique structure of α -MoO₃ integrated with the anhydrous proton transfer mechanism interprets the high-rate decoupled water electrolysis hydrogen production over α -MoO₃, making it stand out among the investigated materials.

Conclusions

To summarize, α -MoO₃ was successfully exploited as a redox mediator for decoupled water electrolysis. The electrochemical measurements of the as-prepared α -MoO₃ in an acidic electrolyte (10 M H₃PO₄) in a three-electrode system disclosed a fast H⁺ transfer and accumulated H⁺ storage in the dense oxide-ion arrays of α -MoO₃. Using an IrO_x anode and a Pt cathode, the decoupled membrane-free water electrolysis over α -MoO₃ as the mediator was successfully demonstrated at various current densities up to 100 A g⁻¹ with high-purity hydrogen product of nearly 100%, which largely outperformed benchmark material Ni(OH)₂ that compromised hydrogen product purity at current rates of > 16 A g⁻¹. The hydrogen production amount with α -MoO₃ redox mediator (ca. 4 mmol H₂ per g(MoO₃) at 100 A g⁻¹) is > 3 times of that with CuFe-TBA. This study demonstrated the decoupled HER and OER with the α -MoO₃ redox mediator as one example of electrocatalytic application, and this decoupled electrolysis can be extended for the systems dealing with alternative counter reactions such as oxidation of liquid fuels (e.g. ethanol and methanol) as a direct fuel cell^{31,34}, and zinc stripping to compose a α -MoO₃-Zn battery^{21,32,35}. Therefore, further exploration on decoupled chemistries with high-rate α -MoO₃ redox mediator would be an important topic in the future.

Experimental

Materials synthesis

α -MoO₃ was synthesized *via* a simple hydrothermal synthesis approach¹⁸, where 2 g of (NH₄)₆Mo₇O₂₄·4H₂O (Wako) was dissolved in 50 mL of water, followed by the addition of 20 mL of HNO₃ solution (3 M). After stirring for 30 min, the transparent colorless solution was poured into a 100 mL TeflonTM-lined Parr autoclave (fill factor: 0.7) and heated at 180 °C for 16 h. After filtration, the white-colored powder was washed with water and ethanol and then dried in an oven at 80 °C in air overnight.

The CuFe-PBA was synthesized *via* a coprecipitate approach, where 40 mL of CuSO₄ solution (0.2M) and 40 mL of K₃Fe(CN)₆ solution (0.1M) was added dropwise to 20 mL of distilled water under stirring. After 6 h of reaction at room temperature, the green precipitate was filtrated and washed with water and ethanol before drying in an oven at 80 °C in air overnight. The battery grade Ni(OH)₂ powder was purchased from Kansai Catalyst Co. and was used as received.

Electrode preparation

The redox mediator electrode for electrochemical characterization was fabricated by slurry casting 70 wt% MoO₃ or CuFe-TBA or Ni(OH)₂ active material, 20 wt% Ketjen-black (ECP-600JD, Lion Corp.) and 10 wt% polyvinylidene difluoride (PVDF) binder on a carbon cloth/Ni felt using prompt amounts of N-methyl-2-pyrrolidone (NMP) (Kanto, 99%) as the solvent. The active materials are ball-milled with Ketjen-black for 30 min prior to slurry making. The loading level of the electrodes was optimized to ~10 mg cm⁻².

The model IrOx and Pt electrodes were prepared by electrochemical deposition following the reported protocol.^{26,36} More specifically, for IrOx electrode, the aged solution at 35 °C for 4 days containing 0.4 mM of Na₃IrCl₆·xH₂O and 2 mM of H₂C₂O₄ with the pH of 10 was used as the electrolyte and titanium felt was employed as the substrate. Prior to the deposition, the Ti felt with a geometric size of 1×1cm² was pretreated by concentrated HCl (ca. 35 wt. %) for 1 min to remove the oxide layer. The electrochemical deposition was conducted using a three-electrode configuration with Pt mesh (Nilaco) and Ag/AgCl (saturated with KCl) as the counter and reference electrodes, respectively. The applied current density was 140 μA cm⁻² for 17.5 h during the electrochemical deposition to obtain the working electrode of IrOx/Ti felt. Regarding the Pt electrode, the procedure was similar. First, the Pt mesh was washed by immersion in aqua regia (HCl/HNO₃ =3 : 1, V/V) for 1 min. Subsequently, Pt was electro-deposited onto the Pt mesh as a working electrode by immersing the mesh in the electrolyte of 0.01 M H₂PtCl₆ and 0.023 M HClO₄ and applying a constant potential of -0.1 V vs. Ag/AgCl for 15 min, named as Pt/Pt mesh.

Electrochemical Measurements

The electrochemical redox properties were examined by cyclic voltammetry (CV) and galvanostatic charge and discharge (GCD) with a BioLogic potentiostat electrochemical workstation. The performance of the decoupled water electrocatalysis was investigated by chronopotentiometry (CP) technique. A custom-made one-chamber cell with 30 mL of 10 M H₃PO₄ was used and a three-electrode cell configuration was obtained. An Ag/AgCl (saturated with KCl) was used as the reference electrode during all the electrochemical measurements. The electrochemical impedance spectroscopy (EIS) data was recorded under an open circuit potential over a frequency range from 0.01 Hz to 100 Hz at the amplitude of the sinusoidal voltage of 5 mV. All experiments were performed at room temperature.

Materials Characterization

Powder XRD and *in situ* XRD studies were conducted with a Rigaku RINT TTR-III (Cu K α radiation). VESTA³⁷ software was used to illustrate the crystal structure.

Gas Detection

Gaseous products were quantified using an in-line mass spectra (MS, INFICON transpector, CPM 3 compact process monitor) system. The carrier gas (Ar) was supplied at a flow rate of 50 mL min⁻¹ to degas the electrolyte and carry out the generated products to MS.

Declarations

Author Contributions

M.O., K.T. and A.Y. conceived and directed the project. Z.M., X.L. and T.S. designed the experiments. Z.M., X.L. and S.P. conducted material synthesis and electrochemical measurements. All authors wrote the manuscript.

Conflicts of Interest

There are no conflicts of interest.

Acknowledgments

This work was financially supported by JST CREST grant no. JPMJCR2106. This work was also supported by the Ministry of Education, Culture, Sports, Science and Technology (MEXT), Japan; Grant-in-Aid for Scientific Research (S) no. 20H05673. M.O. was financially supported by Grant-in-Aid for Scientific Research (A) no. 21H04697 and Grant-in-Aid for Scientific Research on Innovative Areas 19H05816. Z.M. acknowledges the Global Leader Program for Social Design & Management and Japan Society for the Promotion of Science (JSPS) for her grants.

References

1. Abe, J. O., Popoola, A. P. I., Ajenifuja, E. & Popoola, O. M. Hydrogen energy, economy and storage: Review and recommendation. *International Journal of Hydrogen Energy* **44**, 15072–15086 (2019).

2. Turner, J. A. Sustainable Hydrogen Production. *Science* **305**, 972–974 (2004).
3. Trinke, P. *et al.* Hydrogen Crossover in PEM and Alkaline Water Electrolysis: Mechanisms, Direct Comparison and Mitigation Strategies. *J. Electrochem. Soc.* **165**, F502 (2018).
4. Ifkovits, Z. P., Evans, J. M., Meier, M. C., Papadantonakis, K. M. & Lewis, N. S. Decoupled electrochemical water-splitting systems: a review and perspective. *Energy Environ. Sci.* **14**, 4740–4759 (2021).
5. McHugh, P. J., Stergiou, A. D. & Symes, M. D. Decoupled Electrochemical Water Splitting: From Fundamentals to Applications. *Advanced Energy Materials* **10**, 2002453 (2020).
6. Wallace, A. G. & Symes, M. D. Decoupling Strategies in Electrochemical Water Splitting and Beyond. *Joule* **2**, 1390–1395 (2018).
7. Symes, M. D. & Cronin, L. Decoupling hydrogen and oxygen evolution during electrolytic water splitting using an electron-coupled-proton buffer. *Nature Chem* **5**, 403–409 (2013).
8. Choi, B. *et al.* A novel water-splitting electrochemical cycle for hydrogen production using an intermediate electrode. *Chemical Engineering Science* **157**, 200–208 (2017).
9. Wang, J. *et al.* Decoupling half-reactions of electrolytic water splitting by integrating a polyaniline electrode. *J. Mater. Chem. A* **7**, 13149–13153 (2019).
10. Dotan, H. *et al.* Decoupled hydrogen and oxygen evolution by a two-step electrochemical–chemical cycle for efficient overall water splitting. *Nat Energy* **4**, 786–795 (2019).
11. Landman, A. *et al.* Photoelectrochemical water splitting in separate oxygen and hydrogen cells. *Nature Mater* **16**, 646–651 (2017).
12. Oliva, P. *et al.* Review of the structure and the electrochemistry of nickel hydroxides and oxyhydroxides. *Journal of Power Sources* **8**, 229–255 (1982).
13. Barnard, R., Randell, C. F. & Tye, F. L. Studies concerning charged nickel hydroxide electrodes. II. Thermodynamic considerations of the reversible potentials. *J Appl Electrochem* **10**, 127–141 (1980).
14. Trafela, Š., Zavašnik, J., Šturm, S. & Žužek Rožman, K. Controllable voltammetric formation of a structurally disordered NiOOH/Ni(OH)₂ redox pair on Ni-nanowire electrodes for enhanced electrocatalytic formaldehyde oxidation. *Electrochimica Acta* **362**, 137180 (2020).
15. Liang, S., Jiang, M., Luo, H., Ma, Y. & Yang, J. A High-Rate Electrode with Grotthuss Topochemistry for Membrane-Free Decoupled Acid Water Electrolysis. *Advanced Energy Materials* **11**, 2102057 (2021).

16. Agmon, N. The Grotthuss mechanism. *Chemical Physics Letters* **244**, 456–462 (1995).
17. Wu, X. *et al.* Diffusion-free Grotthuss topochemistry for high-rate and long-life proton batteries. *Nature Energy* **4**, 123–130 (2019).
18. Jiang, H. *et al.* A High-Rate Aqueous Proton Battery Delivering Power Below $-78\text{ }^{\circ}\text{C}$ via an Unfrozen Phosphoric Acid. *Advanced Energy Materials* **10**, 2000968 (2020).
19. Guo, H. *et al.* Two-Phase Electrochemical Proton Transport and Storage in $\alpha\text{-MoO}_3$ for Proton Batteries. *Cell Reports Physical Science* **1**, 100225 (2020).
20. Wang, X., Xie, Y., Tang, K., Wang, C. & Yan, C. Redox Chemistry of Molybdenum Trioxide for Ultrafast Hydrogen-Ion Storage. *Angewandte Chemie International Edition* **57**, 11569–11573 (2018).
21. Ma, Z. *et al.* Anhydrous Grotthuss mechanism for fast proton transport in a dense oxide-ion array of $\alpha\text{-MoO}_3$. (2022) doi:10.21203/rs.3.rs-1201760/v1.
22. Bhardwaj, R. C., Enayetullah, M. A. & Bockris, J. O. Proton Activities in Concentrated Phosphoric and Trifluoromethane Sulfonic Acid at Elevated Temperature in Relation to Acid Fuel Cells. *J. Electrochem. Soc.* **137**, 2070–2076 (1990).
23. Su, Z. *et al.* Ultrahigh Areal Capacity Hydrogen-Ion Batteries with MoO_3 Loading Over 90 mg cm^{-2} . *Advanced Functional Materials* **30**, 2005477 (2020).
24. Petit, M. A. & Plichon, V. Anodic electrodeposition of iridium oxide films. *Journal of Electroanalytical Chemistry* **444**, 247–252 (1998).
25. Lee, I., Chan, K.-Y. & Phillips, D. L. Growth of electrodeposited platinum nanocrystals studied by atomic force microscopy. *Applied Surface Science* **136**, 321–330 (1998).
26. Naito, T., Shinagawa, T., Nishimoto, T. & Takanabe, K. Water Electrolysis in Saturated Phosphate Buffer at Neutral pH. *ChemSusChem* **13**, 5921–5933 (2020).
27. Su, Z. *et al.* “Water-in-Sugar” Electrolytes Enable Ultrafast and Stable Electrochemical Naked Proton Storage. *Small* **17**, 2102375 (2021).
28. Liu, Y. *et al.* Interfacial Engineering Coupled Valence Tuning of MoO_3 Cathode for High-Capacity and High-Rate Fiber-Shaped Zinc-Ion Batteries. *Small* **16**, 1907458 (2020).
29. Liu, Y. *et al.* Polypyrrole-coated $\alpha\text{-MoO}_3$ nanobelts with good electrochemical performance as anode materials for aqueous supercapacitors. *J. Mater. Chem. A* **1**, 13582–13587 (2013).
30. Liu, Y. *et al.* A nanocomposite of MoO_3 coated with PPy as an anode material for aqueous sodium rechargeable batteries with excellent electrochemical performance. *Electrochimica Acta* **116**,

512–517 (2014).

31. Ma, Y. *et al.* Combining water reduction and liquid fuel oxidization by nickel hydroxide for flexible hydrogen production. *Energy Storage Materials* **11**, 260–266 (2018).
32. Chen, L., Dong, X., Wang, Y. & Xia, Y. Separating hydrogen and oxygen evolution in alkaline water electrolysis using nickel hydroxide. *Nat Commun* **7**, 11741 (2016).
33. Elbaz, Y., Furman, D. & Toroker, M. C. Hydrogen transfer through different crystal phases of nickel oxy/hydroxide. *Physical Chemistry Chemical Physics* **20**, 25169–25178 (2018).
34. Hamnett, A. Mechanism and electrocatalysis in the direct methanol fuel cell. *Catalysis Today* **38**, 445–457 (1997).
35. Zhang, H. *et al.* Interlayer Engineering of α -MoO₃ Modulates Selective Hydronium Intercalation in Neutral Aqueous Electrolyte. *Angewandte Chemie International Edition* **60**, 896–903 (2021).
36. Naito, T., Shinagawa, T., Nishimoto, T. & Takanabe, K. Gas Crossover Regulation by Porosity-Controlled Glass Sheet Achieves Pure Hydrogen Production by Buffered Water Electrolysis at Neutral pH. *ChemSusChem* **15**, e202102294 (2022).
37. Momma, K. & Izumi, F. VESTA 3 for three-dimensional visualization of crystal, volumetric and morphology data. *J Appl Cryst, J Appl Crystallogr* **44**, 1272–1276 (2011).

Figures

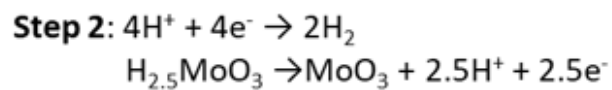
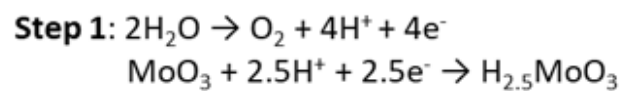
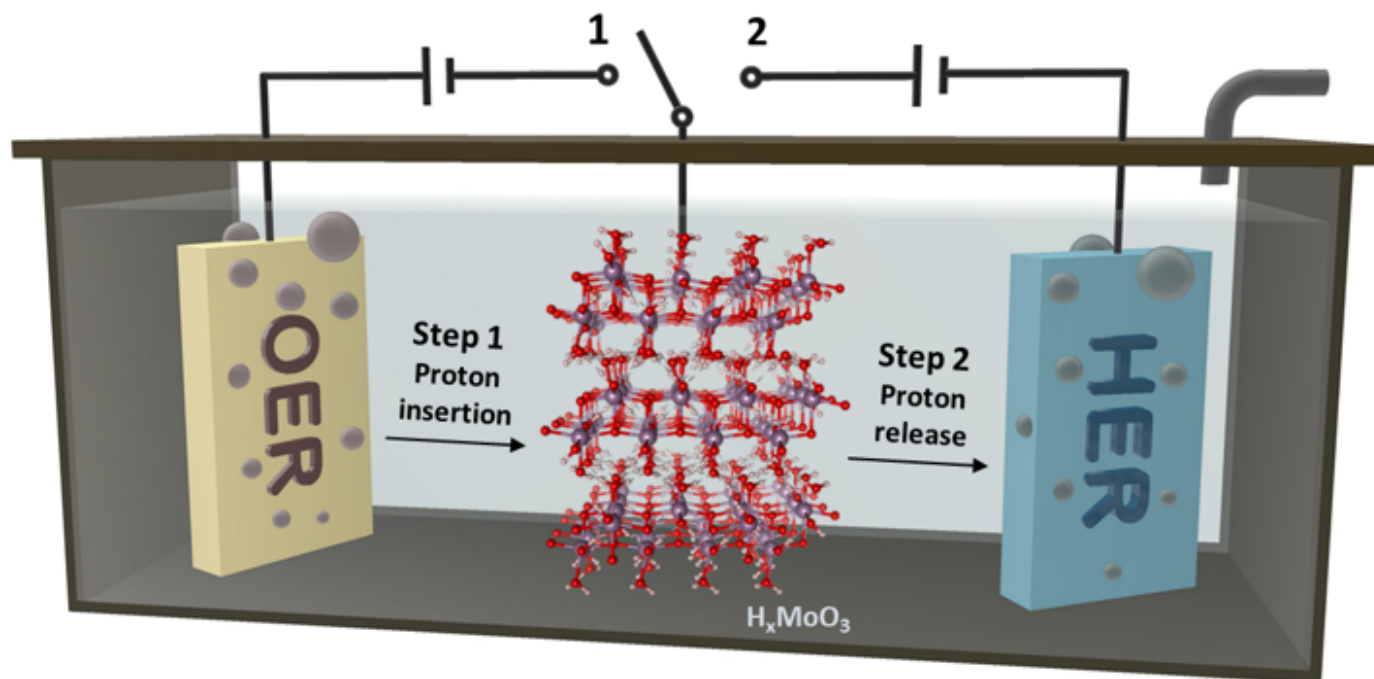


Figure 1

Schematic illustration of the decoupled water electrocatalysis prototype. The prototype consists of a hydrogen evolution reaction electrode (platinized Pt), an oxygen evolution reaction electrode (IrO_x coated Ti felt) and a reversible H⁺ storage redox mediator electrode α-MoO₃ with an aqueous acidic electrolyte.

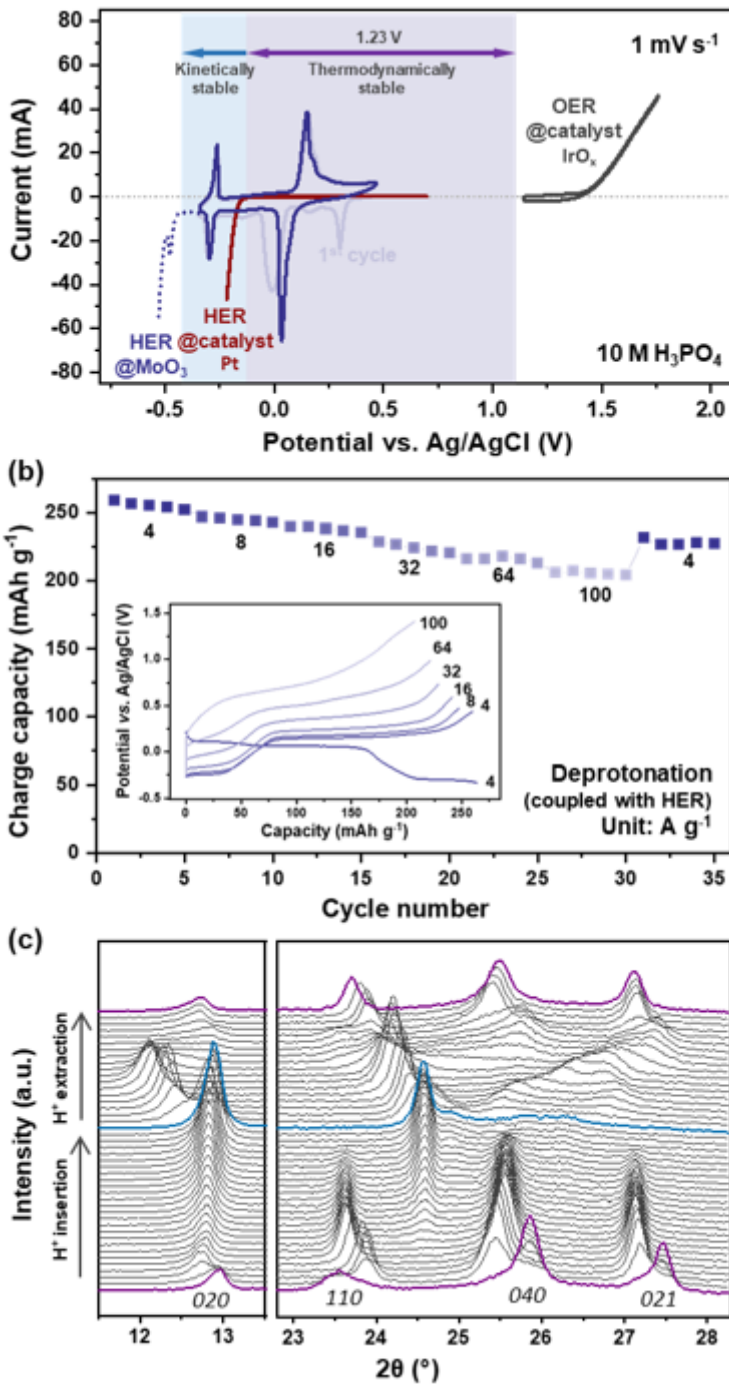


Figure 2

Fast reversible proton storage properties of α - MoO_3 . (a) cyclic voltammetry (CV) curves of α - MoO_3 (pale blue line: first cycle, dark blue line: subsequent cycles). The CV curves of hydrogen evolution on Pt catalyst (red line) and oxygen evolution on IrO_x catalyst (dark gray lines) are also shown for comparison. The blue dotted lines are the linear sweep voltammetry (LSV) curve using the α - MoO_3 electrode. (b) Rate performance of α - MoO_3 at charge rate from 4 A g^{-1} to 100 A g^{-1} . Inset: the charge curves of α - MoO_3 at different rates, corresponding to H_xMoO_3 ($1 \leq x \leq 2.5$), a discharge curve at rate of 4 A g^{-1} is also shown

for comparison. (c) Lattice response of MoO_3 upon galvanostatic proton insertion and extraction (100 mA g^{-1}) via in situ X-ray diffraction (XRD) method.

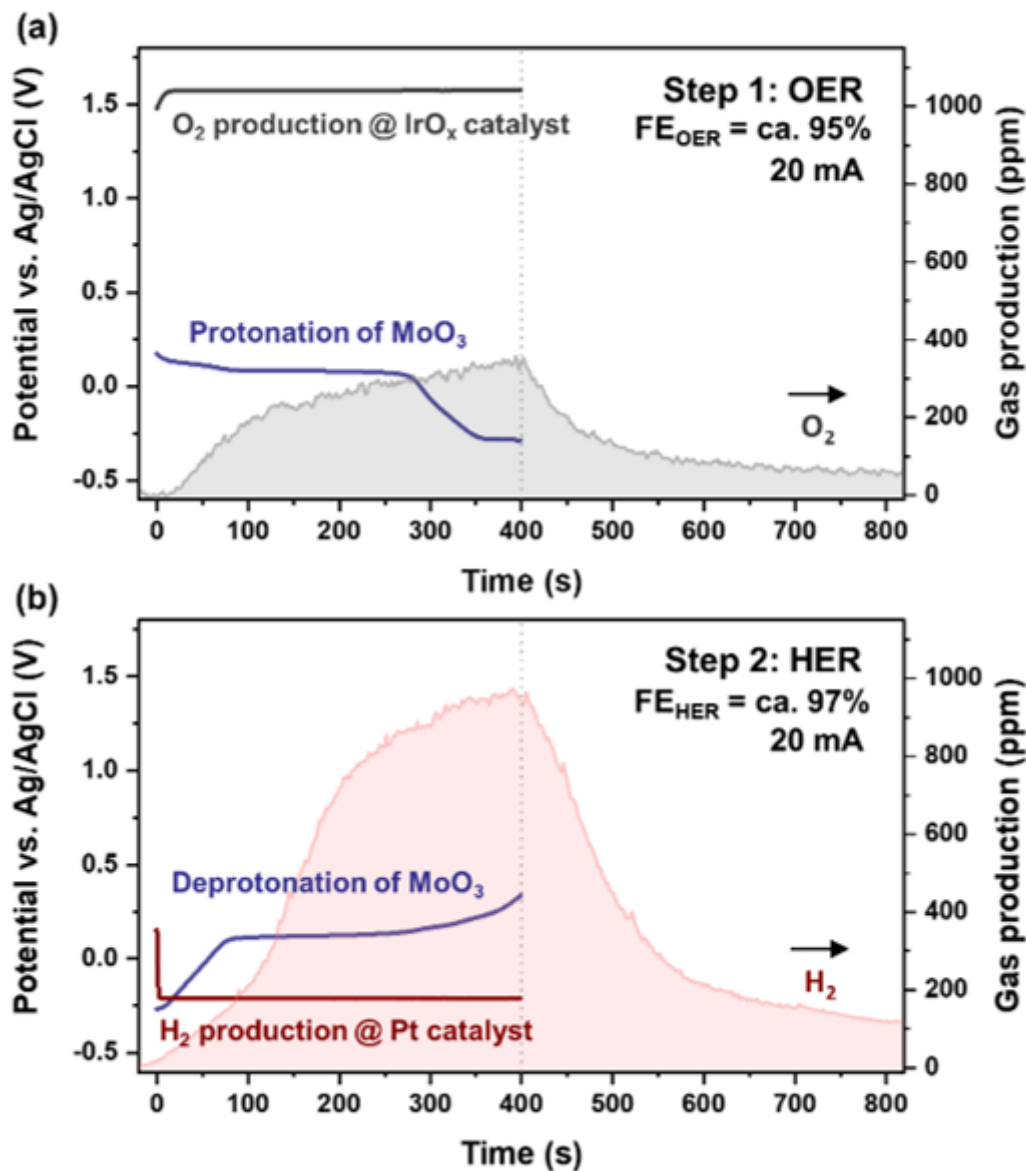


Figure 3

Decoupled hydrogen and oxygen evolution with MoO_3 redox mediator. Chronopotentiometry curves of (a) oxygen evolution reaction (OER) step and (b) hydrogen evolution reaction (HER) step. The potentials of OER electrode (dark gray line), HER electrode (red line) and $\alpha\text{-MoO}_3$ redox mediator electrode (blue lines) were recorded at a current rate of 20 mA with a step duration of 400 s. The oxygen (gray area) and hydrogen production (pink area) concentration detected by mass spectroscopy are also recorded.

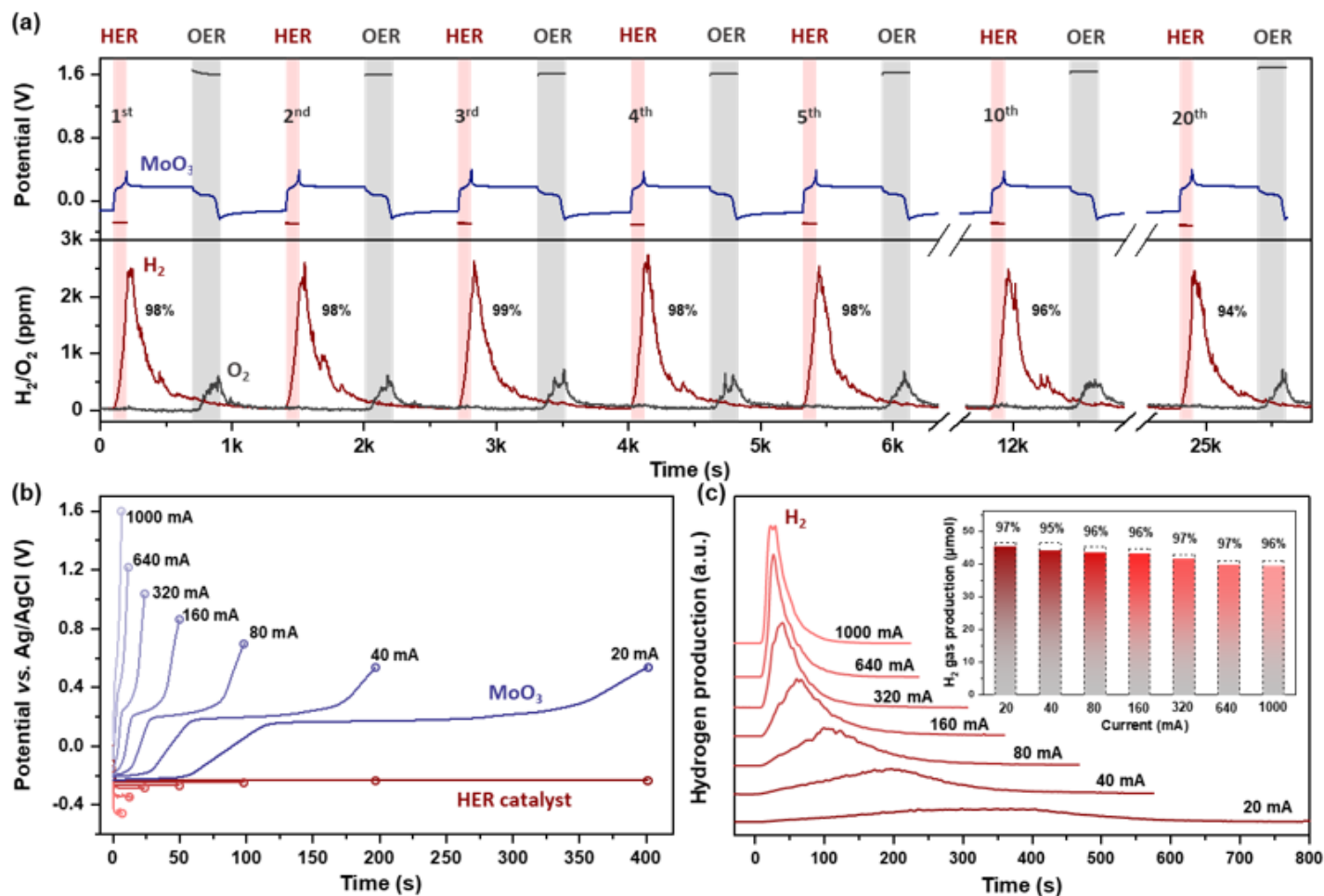


Figure 4

Fast hydrogen production. (a) Twenty consecutive OER/HER cycles. The current for HER step was 80 mA for 100 s, the current for OER step was 40 mA for 200 s, each step is followed with a rest of 500 s. The first 5 cycles, the 10th and the 20th cycles are shown. (b) Chronopotentiometry curves of α - MoO_3 redox mediator electrode and HER catalyst electrode at rates from 20 mA cm⁻² to 1 A cm⁻² and (c) corresponding H_2 gas production deduced from mass spectroscopy signals. Inset: theoretical hydrogen gas amount (red solid bars) and detected gas amount (dash squares), the corresponding Faradic efficiency was marked at the top of each bar.

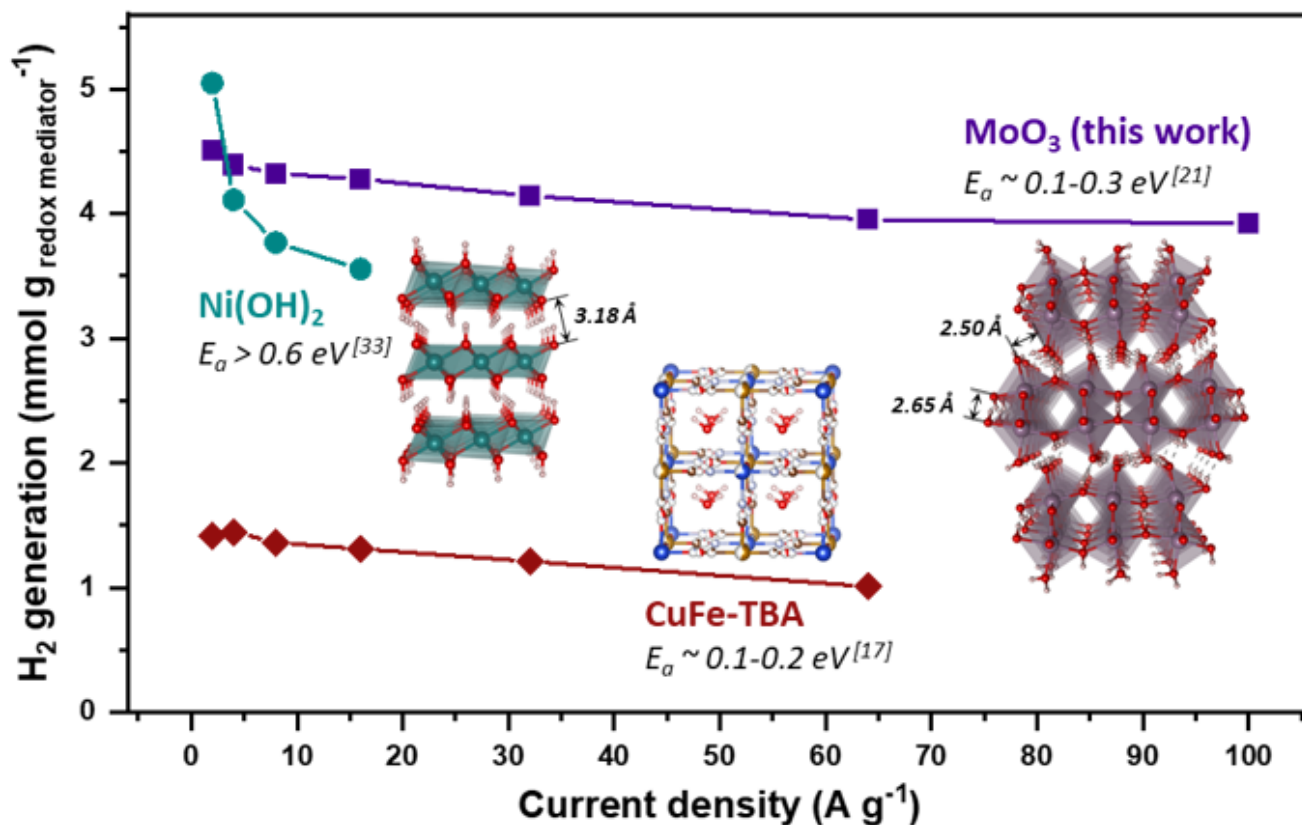


Figure 5

A fast hydrogen production performance comparison of α -MoO₃ with other benchmark redox mediators. The performance of Ni(OH)₂ and CuFe-TBA was evaluated with the same set-up. 10 mg of each active material casted on a carbon paper of 1 cm² was tested. The electrolytes used for CuFe-TBA, and Ni(OH)₂ are 10 M H₃PO₄ and 1 M KOH, respectively. Note that the structure of CuFe-TBA shown in the figure is schematic, the actual structural water amount is larger than that is shown.

Supplementary Files

This is a list of supplementary files associated with this preprint. Click to download.

- [watersplittingsupportingnc.docx](#)